Topological Marker Currents in Chern Insulators

M. D. Caio,[1] G. Möller,[2] N. R. Cooper,[3] and M. J. Bhaseen[4]

[1] *Instituut-Lorentz, Universiteit Leiden, P.O. Box 9506, 2300 RA Leiden, The Netherlands*
[2] *Functional Materials Group, School of Physical Sciences, University of Kent, Kent CT2 7NZ, United Kingdom*
[3] *T.C.M. Group, Cavendish Laboratory, J.J. Thomson Avenue, Cambridge CB3 0HE, United Kingdom*
[4] *Department of Physics, King's College London, Strand, London WC2R 2LS, United Kingdom*

Topological states of matter exhibit many novel properties due to the presence of robust topological invariants such as the Chern index. These global characteristics pertain to the system as a whole and are not locally defined. However, local topological markers can distinguish between topological phases, and they can vary in space. In equilibrium, we show that the topological marker can be used to extract the critical behaviour of topological phase transitions. Out of equilibrium, we show that the topological marker spreads via a flow of currents emanating from the sample boundaries, and with a bounded maximum propagation speed. We discuss the possibilities for measuring the topological marker and its flow in experiment.

PACS numbers: 03.65.Vf, 67.85.-d, 73.43.-f, 73.43.Nq, 71.10.Fd

Topological quantum systems exhibit many striking phenomena due to the inherent topological properties of their ground state wavefunctions. Experimental signatures in two-dimensions include the robust quantisation of the transverse charge transport, with direct links to topological invariants [1]. The observation of the Quantum Hall Effect in graphene highlights that topology can be relevant at room temperature [2], widening the scope for practical applications. The recent discovery of topological insulators [3–5] extends the reach of topology to a wider class of materials and dimensionalities, giving rise to exotic phases such as topological superconductors [6]. Discoveries of topological phases in photonic systems [7–11] and cold atomic gases [12–21] have expanded the range of experimental probes and measurement techniques, providing access to a much broader range of physical observables. These diverse systems could also play an important role in fault tolerant quantum information processing [22].

Recently, the behaviour of non-equilibrium topological systems has come under scrutiny, with a view towards the time-dependent interrogation and manipulation of their novel topological properties. Theoretical studies include quantum quenches in $p+ip$ superfluids [23, 24] and Chern insulators [25, 26]. Non-equilibrium dynamics of topological systems has also been examined in the context of periodically driven Floquet systems [27–31], as recently realised in experiment [14]. A notable finding is that global topological invariants are preserved under unitary evolution [23–25, 27], unless dynamically-induced symmetry breaking takes place [32]. However, local physical observables, such as the magnetisation, can change [25]. In addition, the Hall response is no longer quantised, and undergoes temporal dynamics [26, 28–30].

In this work, we examine the equilibrium and non-equilibrium properties of Chern insulators from the vantage point of the real-space topological marker [34]. We show that the topological marker can be used to extract the critical behaviour of topological phase transitions, in spite of the fact that no traditional local order parameter exists. Out of equilibrium, we show that the topological marker spreads via a flow of currents, with a maximum propagation speed that is determined by the band structure of the final Hamiltonian. In finite-size samples, these currents emanate from the sample boundaries. We discuss the relevance of these findings to experiment.

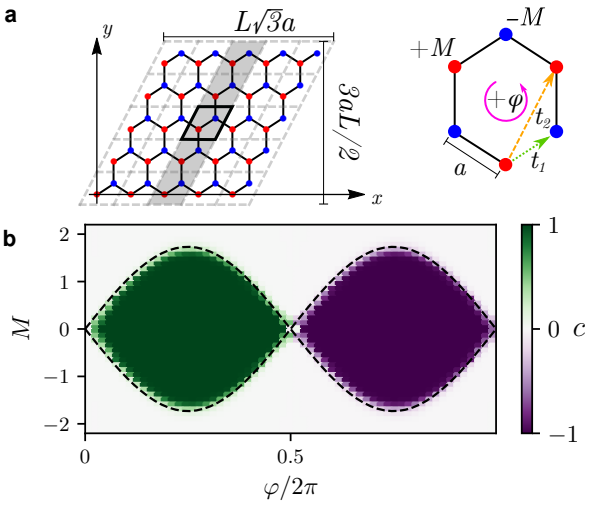

Figure 1. **Lattice geometry and phase diagram. a** Lattice geometry of the Haldane model. We consider a diamond-shaped sample (light grey) with edges composed of L unit cells along primitive lattice vectors, and $N = 2L^2$ sites. **b** Density plot of the Chern marker (3) in the central cell (bold) in panel **a**, with $L = 17$. The dashed lines are the phase boundaries $M = \pm\sqrt{3}\sin\varphi$ of the Haldane model [33] with $t_1 = 1$, $t_2 = 1/3$ and $a = 1$.

Model. In order to expose the applications of the topological marker, we focus on the Haldane model [33]. This model is celebrated for realising topological bands

without an external magnetic field, as recently exploited in cold atomic gas experiments [12, 14]. It also played an important role in the discovery of topological insulators [35]. The Hamiltonian describes spinless fermions on a honeycomb lattice

$$\hat{H} = -t_1 \sum_{\langle i,j \rangle} \left(\hat{c}_i^\dagger \hat{c}_j + \text{h.c.} \right) - t_2 \sum_{\langle\langle i,j \rangle\rangle} \left(e^{\mathrm{i}\varphi_{ij}} \hat{c}_i^\dagger \hat{c}_j + \text{h.c.} \right) + M \sum_{i \in A} \hat{n}_i - M \sum_{i \in B} \hat{n}_i, \quad (1)$$

where the fermionic creation and annihilation operators $\hat{c}_i^\dagger$ and $\hat{c}_i$ obey anticommutation relations $\{\hat{c}_i, \hat{c}_j^\dagger\} = \delta_{ij}$, and $\hat{n}_i \equiv \hat{c}_i^\dagger \hat{c}_i$; see Fig. 1a. Here, t_1 and t_2 are the first and second neighbour hopping amplitudes, and the angular brackets $\langle\rangle$ and $\langle\langle\rangle\rangle$ indicate summation over the first and second neighbour pairs respectively. The parameter M breaks the inversion symmetry between the A and B sublattices, as indicated by the red and blue dots in Fig. 1a, yielding a trivial insulating phase for sufficiently large M. The phase $\varphi_{ij} = \pm\varphi$ breaks time-reversal symmetry, and is positive (negative) for anticlockwise (clockwise) second neighbor hopping, as shown in Fig. 1a. This allows for topological phases at half-filling, even without a net magnetic field [33]. The phases are distinguished by the Chern index, which is a global property of a band of Bloch states $|\psi(\mathbf{k})\rangle$:

$$C = \frac{1}{2\pi} \int_{\text{BZ}} d^2k \; \Omega, \quad (2)$$

where $\Omega = \partial_{k_x} A_{k_y} - \partial_{k_y} A_{k_x}$ is the Berry curvature, $A_{k_\mu} = i\langle\psi(\mathbf{k})|\partial_{k_\mu}|\psi(\mathbf{k})\rangle$ is the Berry connection, and the integral is over the 2D Brillouin zone. The Chern index thereby characterises the topology of the band of states $|\psi(\mathbf{k})\rangle$ and is robustly quantised. For the ground state of the Haldane model at half-filling, $C = \pm 1$ in the topological phases and $C = 0$ in the non-topological phase; see Fig. 1b. Throughout the manuscript, we fix the hoppings $t_1 = 1$, $t_2 = 1/3$, and the lattice spacing $a = 1$.

Local Chern Marker. In open-boundary systems, or in the presence of disorder, the lack of translational invariance renders the expression (2) undefined. Recently, the notion of a local Chern marker has been introduced [34], with the explicit representation

$$c(\mathbf{r}_\alpha) = -\frac{4\pi}{A_c} \text{Im} \sum_{s=A,B} \langle \mathbf{r}_{\alpha_s} | \hat{P}\hat{x}\hat{Q}\hat{y}\hat{P} | \mathbf{r}_{\alpha_s} \rangle, \quad (3)$$

where A_c is the area of a real-space unit cell, $\hat{P}$ is the projector onto the ground state, and $\hat{Q} = \hat{I} - \hat{P}$ is the complementary projector. The sum is over the two sublattice sites $s = A, B$ within the unit cell α, and $|\mathbf{r}_i\rangle = \hat{c}_i^\dagger |0\rangle$ is the state localised on the corresponding site $i \equiv \alpha_s$. Owing to the shortsightedness of $\hat{P}$ for gapped phases [36], the topological marker defined in Eq. (3) has a quasi-local character [37, 38]; for Chern insulators, $\hat{P}$ is exponentially localised in the gapped bulk, but has extended support along the sample boundaries. In order to orient the subsequent discussion, in Fig. 1b, we show the phase diagram of the Haldane model (1) obtained from the real-space Chern marker (3); see also Ref. [34]. The Chern marker clearly discriminates between the topological and non-topological phases [34], in accordance with the phase diagram obtained from the low-energy Dirac theory [33]. In finite-size samples, the Chern marker averages to zero, but in the interior of the sample it nonetheless distinguishes between topological and non-topological phases [34]. For recent applications of the Chern marker in clean and disordered samples see Refs. [39–43].

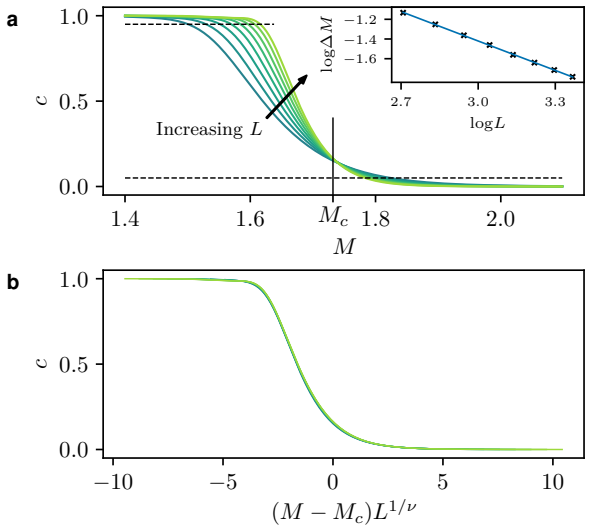

Figure 2. **Scaling of the Chern marker.** **a** Vertical slice through the phase diagram in Fig. 1b with $\varphi = \pi/2$, showing the variation of the local Chern marker in the centre of the sample as a function of M. The results smoothly interpolate between 1 and 0 in the vicinity of the topological phase transition. The different curves correspond to increasing system sizes $L = 15, 17, 19, 21, 23, 25, 27, 29$, as illustrated. The curves cross in a narrow region within 0.5% of $M_c = \sqrt{3}$, the exact transition point of the Haldane model for the chosen parameters. The width ΔM of the transition region, corresponding to the interval from $c = 0.95$ to $c = 0.05$ (horizontal lines), scales as $\Delta M \sim L^{-1/\nu}$. Inset: linear plot showing $\nu = 0.995(6) \approx 1$. This is consistent with the correlation length exponent in the low-energy Dirac theory. **b** Re-plotting the data in panel **a** as $c \sim \tilde{f}((M - M_c)L^{1/\nu})$ with $\nu = 1$ yields scaling collapse.

Critical Properties. Inspection of the phase diagram in Fig. 1b highlights that, away from the phase boundaries, the local Chern marker is $0, \pm 1$ within machine precision. However, in the vicinity of the transition for finite-size samples, c is no longer quantised [34]. In Fig. 2a, we show the variation of the Chern marker as

one passes between the topological and non-topological phases. It can be seen that the transition region narrows with increasing system size, suggesting a sharp discontinuity in the thermodynamic limit. Assuming that the departure from quantisation in the middle of the sample occurs when the bulk correlation length ξ (or alternatively, the edge penetration depth) is of order (half the) system size, finite-size effects become relevant when $\xi \sim L/2$. Further assuming that $\xi \sim (\Delta M)^{-\nu}$, where ΔM is the width of the transition region in Fig. 2a and ν is the correlation length exponent, one expects that the width scales with the system size according to $\Delta M \sim L^{-1/\nu}$. In the inset of Fig. 2a we confirm this dependence, with $\nu = 0.995(6) \approx 1$. This is consistent with the correlation length exponent of the low-energy Dirac theory [44]. It is also compatible with the delocalisation of the edge states into the interior of the sample on closing the gap. Re-plotting the data in Fig. 2a with the scaling form $c \sim f(\xi/L) = f((M - M_c)^{-\nu}/L) = \tilde{f}((M - M_c)L^{1/\nu})$ with $\nu = 1$, shows that the data collapse onto a single curve; see Fig. 2b. This confirms that the real-space Chern marker can be used to extract the critical behaviour of topological phase transitions, in a similar way to a local order parameter for conventional phase transitions. In contrast to approaches using the momentum space Berry curvature [45, 46], the present technique can be applied in non-translationally invariant settings.

Non-Equilibrium Dynamics. Having exposed the equilibrium properties of the Chern marker, we turn our attention to its non-equilibrium dynamics. Here, we focus on quantum quenches, where the system is prepared in the ground state $|\psi_0(M, \varphi)\rangle$ of the initial Hamiltonian $\hat{H}(M, \varphi)$ at half-filling and, upon sudden change of the parameters to new values (M', φ'), it evolves as $\exp[-i\hat{H}(M', \varphi')t]|\psi_0(M, \varphi)\rangle$. The Chern marker is evaluated using Eq. (3), and the projector onto the time evolving state [40]. In Fig. 3a, we show the dynamics of the Chern marker, evaluated in the centre of a finite-size sample, following quenches for different starting points in the topological phase to a fixed parameter point in the non-topological phase. For these quenches, the Chern marker initially remains quantised, but it departs from quantisation after a characteristic timescale t^*, that is independent of the initial Hamiltonian parameters. As we shall discuss in more detail below, this timescale is consistent with a flow of Chern marker currents, from the vicinity of the sample boundaries towards the interior. Evidence for the propagation of these currents can be seen in real-space plots of $c(\mathbf{r})$ along a cut through the centre of the sample, as indicated by the grey shaded region in Fig. 1a. The Chern marker, which is initially negative near the sample boundaries (to ensure that $c(\mathbf{r})$ integrates to zero) flows from the edges towards the interior; see Fig. 3b. Probing the time at which c departs from unity, in the middle of a sample for different system sizes L, allows us to estimate the speed of propagation, as illustrated in Fig. 3c. In addition to a well-defined propagation speed v, it is evident that the disturbance emanates from the vicinity of the edges, where y_0 is the finite width of the edge at equilibrium; see Fig. 3b.

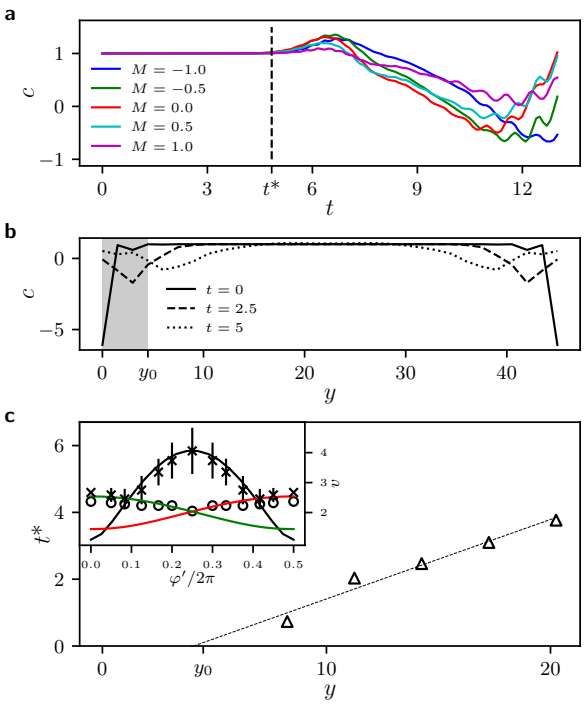

Figure 3. **Non-equilibrium dynamics.** **a** Time-evolution of the Chern marker in the centre of a sample with $L = 31$, following quenches from different points in the topological phase with $M = -1, -0.5, 0, 0.5, 1$, to the non-topological phase with $M' = 5$, and $\varphi = \pi/2$ held fixed. The Chern marker remains quantised until a characteristic time t^*, which is independent of the initial parameters. **b** Spatial profile of $c(\mathbf{r})$ along a cut corresponding to the shaded area in Fig. 1a, where y is the vertical distance from the horizontal boundary, as indicated in Fig. 1a. Explicitly, $y = 3a\ell/2$ where ℓ counts the number of unit cells from the lower boundary, and $a = 1$. The results are shown at times $t = 0$ (solid), 2.5 (dashed), 5 (dotted), following a quench from $M = 0$ to $M' = 5$, with $\varphi = \pi/2$ held fixed. At $t = 0$, the edge has a width $y_0 \sim 4.5$ (shaded). As t increases, a wave-like disturbance in $c(\mathbf{r})$ propagates into the interior. **c** Dependence of t^* on y, for $L = 11, 15, 19, 23, 27$, for the quench considered in **b**. A linear fit yields a propagation speed $v \sim 4.06 \pm 0.77$; the y-intercept $y \sim 4.4 \pm 2.0$, is close to the initial width of the edge. Inset: variation of v with the parameter φ' of the final Hamiltonian, with $M' = 5$ and initial parameters $\varphi = \pi/2$ and $M = 0$. The speed v (crosses) corresponds to the maximum speed permitted by the final band structure. It coincides with the maximum of $v_1^y(\mathbf{k}) = \partial E_1(\mathbf{k})/\partial k_y$ (red), $v_2^y(\mathbf{k}) = \partial E_2(\mathbf{k})/\partial k_y$ (green) or $|v_2^y(\mathbf{k}) - v_1^y(\mathbf{k})|$ (black), extremised over $\mathbf{k}$-space, where $E_1(\mathbf{k})$ and $E_2(\mathbf{k})$ are the energies of the lower and upper bands respectively; see text. For comparison, we show the speed corresponding to the onset of charge density disturbances (circles) in the centre of the sample.

Propagation Speed. In the inset of Fig. 3c we show the non-trivial variation of v for quenches to different points in the phase diagram. It can be seen that v coincides with the maximum speed (in this case in the y-direction) allowed by the band structure, where we measure speeds in units of $at_1/\hbar$. Depending on the final parameters this is either the maximum speed permitted by the upper and lower bands, or the maximum of the relative band velocities, extremised over $\mathbf{k}$-space. The latter is attributed to coherent particle-hole excitations following the quench, and the presence of the excited state projector $\hat{Q} = \hat{I} - \hat{P}$ in the definition (3), yielding interference terms oscillating at the frequency of the band gap $\Delta(\mathbf{k}) = E_2(\mathbf{k}) - E_1(\mathbf{k})$. Due to this interference, the associated propagation speed of the Chern marker can be larger than the individual band speeds (e.g. if the bands have slopes with opposite signs) as shown in the inset of Fig. 3c. In contrast, the electrical charge density responds on a timescale corresponding to the maximum speed of the individual bands, as shown by the circles in the inset of Fig. 3c; the two-band interference region in the vicinity of $\varphi' = \pi/2$ is absent.

Topological Marker Currents. Further evidence for the propagation of Chern marker currents can also be obtained from the dynamics of $c(\mathbf{r})$ close to the sample edges. For a finite-size sample with open boundaries, $\int c(\mathbf{r}) d^2r = 0$ at all times. A local Chern current $\mathbf{J}_c$ therefore exists, such that $\frac{\partial c}{\partial t} + \nabla \cdot \mathbf{J}_c = 0$. In integral form, the flux of the Chern current $\mathcal{F}_c$ out of a unit cell is given by

$$\mathcal{F}_c := \oint_{\partial A_c} \mathbf{J}_c \cdot d\mathbf{l} = -\int_{A_c} \frac{\partial c}{\partial t}\, d^2r, \tag{4}$$

where A_c and ∂A_c are the area and perimeter of a unit cell. In Fig. 4a, we plot the right hand side of Eq. (4), corresponding to the integrated flux of $\mathbf{J}_c$ through the perimeter of a unit cell, at different spatial positions along a cut through the sample, as illustrated in Fig. 1a. The onset of a non-vanishing flux $\mathcal{F}_c$ occurs at later times with increasing distance from the boundaries. The associated propagation speed v can be extracted from a linear fit of the onset time versus distance, as shown in Fig. 4b. In the inset of Fig. 4b we plot v as a function of the initial parameters for a fixed final Hamiltonian. The extracted speed is approximately independent of the initial starting parameters, and agrees with the speed obtained via the analysis of Fig. 3. In this particular case, the speed v is consistent with the maximum value of $|v_2^y(\mathbf{k}) - v_1^y(\mathbf{k})|$ for the final band structure, which exceeds the maximum speed of each band separately. In Fig. 4c, we show the time evolution of the Chern marker at the mid-point of the bottom edge of the sample. Due to the propagation of Chern marker currents from the boundaries, the Chern marker approaches a steady state value that is close to (but not equal to) zero, corresponding to an excited state of the post-quench Hamiltonian. This steady state is ultimately destabilised due to the onset of finite-size effects.

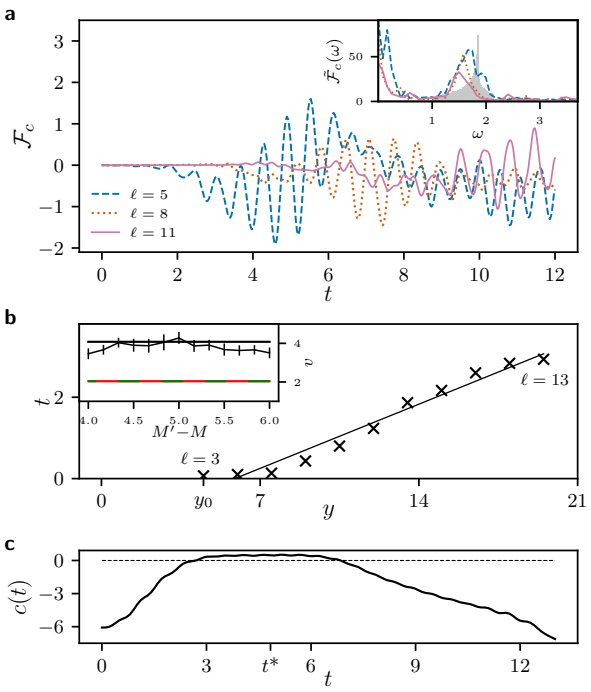

Figure 4. **Topological marker currents.** **a** Flux of the Chern current $\mathcal{F}_c$ through a unit cell distant $\ell = 5$ (dashed), 8 (dotted), and 11 (solid) unit cells from the boundary of a sample with $L = 31$, following a quench from $M = 0$ to $M' = 5$, with $\varphi = \pi/2$ held fixed. The flux departs from zero at later times as ℓ increases, corresponding to the propagation of Chern currents from the edges. Inset: Fourier transform $\tilde{\mathcal{F}}_c(\omega)$ of the data. The characteristic oscillation frequency range corresponds to the distribution of the band gap frequencies $(E_2(k) - E_1(k))/2\pi$ (shaded). **b** Onset time of $\mathcal{F}_c \neq 0$ versus $y = 3/2\,\ell$, for $\ell = 3, 4, 5, \ldots 13$. A linear fit yields a speed v, corresponding to the maximum speed allowed by the final band structure. The y-intercept is compatible with the initial edge width, y_0. Inset: Variation of the speed v for quenches from different points in the phase diagram with $M \in [-1, 1]$ to $M' = 5$, with $\varphi = \pi/2$ held fixed. The speed is consistent with the maximum of $|v_2^y(\mathbf{k}) - v_1^y(\mathbf{k})|$ allowed by the final band structure (solid line), and exceeds the maximum speed of each band separately (red and green lines). **c** Time-dependence of the Chern marker at the mid-point of the sample edge, following the quench in panel **a**. The Chern marker reaches a steady-state value that is close to, but not equal to, zero. The plateau is subsequently destabilised due to the onset of finite-size effects.

Experiment. Although the definition of the Chern marker (2) may appear complicated, its static and dynamic properties could be accessible in experiment. This could be done via measurements of the projection operator $\hat{P}$, as recently performed in photonic topological systems in a real-space basis [47], and in gyroscopic systems [48]. The projector could also be measured using

quantum gas microscopes [49], based on recent proposals to extract the single-particle density matrix [50]. Explicitly, this can be seen by inserting complete set of states $\sum_{\gamma,s} |r_{\gamma_s}\rangle\langle r_{\gamma_s}| = \hat{I}$ into Eq. (3), and noting that the matrix elements of the projector $P_{\alpha_s\beta_{s'}} = \langle r_{\alpha_s}|\hat{P}|r_{\beta_{s'}}\rangle = \sum_{E_k<E_F}\langle r_{\alpha_s}|\psi_k\rangle\langle\psi_k|r_{\beta_{s'}}\rangle$ are those of the single-particle density matrix. The evaluation of $c(\mathbf{r}_\alpha)$ follows, as $|r_{\gamma_s}\rangle$ is a natural basis for the operators $\hat{x}$ and $\hat{y}$. In equilibrium, the Chern marker is also related to the local magnetisation [51], allowing further possibilities for experimental investigation [52].

Conclusions. In this work we have examined the equilibrium and non-equilibrium properties of the real-space Chern marker. In equilibrium, we have shown that it can be used to extract the critical properties of topological phase transitions, in a similar way to a local order parameter for conventional transitions. Out of equilibrium, $c(\mathbf{r})$ undergoes dynamics, giving rise to a flow of topological marker currents with a bounded propagation speed. There are many directions for theory and experiment, including the impact of disorder and interactions on the flow of topological marker currents, and their realisations in other settings. In particular, it would be interesting to understand if the Chern marker currents can be Anderson localised in the presence of disorder, and how their speed of propagation is influenced by the presence of interactions. It would also be interesting to explore the possibilities for manipulating these currents: can they be gated and steered, and can novel devices exploit them?

Data availability. The data presented in Figures 1b, 2, 3, and 4 can be reproduced from the equations in the main text.

[1] D. J. Thouless, *Topological Quantum Numbers in Nonrelativistic Physics* (World Scientific, 1998).
[2] K. S. Novoselov, Z. Jiang, Y. Zhang, S. V. Morozov, H. L. Stormer, U. Zeitler, J. C. Maan, G. S. Boebinger, P. Kim, and A. K. Geim, Science **315**, 1379 (2007).
[3] B. A. Bernevig, T. L. Hughes, and S.-C. Zhang, Science **314**, 1757 (2006).
[4] M. König, S. Wiedmann, C. Brüne, A. Roth, H. Buhmann, L. W. Molenkamp, X.-L. Qi, and S.-C. Zhang, Science **318**, 766 (2007).
[5] L. Fu, C. L. Kane, and E. J. Mele, Phys. Rev. Lett. **98**, 106803 (2007).
[6] M. Sato and Y. Ando, Reports Prog. Phys. **80**, 076501 (2017).
[7] I. Carusotto and C. Ciuti, Rev. Mod. Phys. **85**, 299 (2013).
[8] L. Lu, J. D. Joannopoulos, and M. Soljačić, Nat. Photonics **8**, 821 (2014).
[9] M. Fitzpatrick, N. M. Sundaresan, A. C. Y. Li, J. Koch, and A. A. Houck, Phys. Rev. X **7**, 011016 (2017).
[10] K. Le Hur, L. Henriet, A. Petrescu, K. Plekhanov, G. Roux, and M. Schiró, Comptes Rendus Phys. **17**, 808 (2016).
[11] C. Noh and D. G. Angelakis, Reports Prog. Phys. **80**, 016401 (2017).
[12] J. Dalibard, F. Gerbier, G. Juzelinas, and P. Öhberg, Rev. Mod. Phys. **83**, 1523 (2011).
[13] H. Miyake, G. A. Siviloglou, C. J. Kennedy, W. C. Burton, and W. Ketterle, Phys. Rev. Lett. **111**, 185302 (2013).
[14] G. Jotzu, M. Messer, R. Desbuquois, M. Lebrat, T. Uehlinger, D. Greif, and T. Esslinger, Nature **515**, 237 (2014).
[15] N. Goldman, G. Juzelinas, P. Öhberg, and I. B. Spielman, Reports Prog. Phys. **77**, 126401 (2014).
[16] M. Aidelsburger, M. Lohse, C. Schweizer, M. Atala, J. T. Barreiro, S. Nascimbène, N. R. Cooper, I. Bloch, and N. Goldman, Nat. Phys. **11**, 162 (2014).
[17] M. Lohse, C. Schweizer, O. Zilberberg, M. Aidelsburger, and I. Bloch, Nat. Phys. **12**, 350 (2015).
[18] C. Schweizer, M. Lohse, R. Citro, and I. Bloch, Phys. Rev. Lett. **117**, 170405 (2016).
[19] N. Goldman, G. Jotzu, M. Messer, F. Görg, R. Desbuquois, and T. Esslinger, Phys. Rev. A **94**, 043611 (2016).
[20] N. Goldman, J. C. Budich, and P. Zoller, Nat. Phys. **12**, 639 (2016).
[21] S. Mukherjee, A. Spracklen, M. Valiente, E. Andersson, P. Öhberg, N. Goldman, and R. R. Thomson, Nat. Commun. **8**, 13918 (2017).
[22] C. Nayak, S. H. Simon, A. Stern, M. Freedman, and S. Das Sarma, Rev. Mod. Phys. **80**, 1083 (2008).
[23] M. S. Foster, M. Dzero, V. Gurarie, and E. A. Yuzbashyan, Phys. Rev. B **88**, 104511 (2013).
[24] M. S. Foster, V. Gurarie, M. Dzero, and E. A. Yuzbashyan, Phys. Rev. Lett. **113**, 076403 (2014).
[25] M. D. Caio, N. R. Cooper, and M. J. Bhaseen, Phys. Rev. Lett. **115**, 236403 (2015).
[26] M. D. Caio, N. R. Cooper, and M. J. Bhaseen, Phys. Rev. B **94**, 155104 (2016).
[27] L. D'Alessio and M. Rigol, Nat. Commun. **6**, 8336 (2015).
[28] P. Wang and S. Kehrein, New J. Phys. **18**, 053003 (2016).
[29] P. Wang, M. Schmitt, and S. Kehrein, Phys. Rev. B **93**, 085134 (2015).
[30] H. Dehghani and A. Mitra, Phys. Rev. B **93**, 205437 (2016).
[31] D. J. Yates, Y. Lemonik, and A. Mitra, Phys. Rev. B **94**, 205422 (2016).
[32] M. McGinley and N. R. Cooper, arXiv:1804.05756.
[33] F. D. M. Haldane, Phys. Rev. Lett. **61**, 2015 (1988).
[34] R. Bianco and R. Resta, Phys. Rev. B **84**, 241106 (2011).
[35] C. L. Kane and E. J. Mele, Phys. Rev. Lett. **95**, 226801 (2005).
[36] W. Kohn, Phys. Rev. Lett. **76**, 3168 (1996).
[37] R. Resta, J. Chem. Phys. **124**, 104104 (2006).
[38] R. Resta, Eur. Phys. J. B **79**, 121 (2011).
[39] D.-T. Tran, A. Dauphin, N. Goldman, and P. Gaspard, Phys. Rev. B **91**, 085125 (2015).
[40] L. Privitera and G. E. Santoro, Phys. Rev. B **93**, 241406 (2016).
[41] D. T. Tran, A. Dauphin, A. G. Grushin, P. Zoller, and N. Goldman, Sci. Adv. **3**, e1701207 (2017).
[42] A. Marrazzo and R. Resta, Phys. Rev. B **95**, 121114

(2017).
[43] A. Amaricci, L. Privitera, F. Petocchi, M. Capone, G. Sangiovanni, and B. Trauzettel, Phys. Rev. B **95**, 205120 (2017).
[44] A. W. W. Ludwig, M. P. A. Fisher, R. Shankar, and G. Grinstein, Phys. Rev. B **50**, 7526 (1994).
[45] W. Chen, M. Legner, A. Rüegg, and M. Sigrist, Phys. Rev. B **95**, 075116 (2017).
[46] S. Kourtis, T. Neupert, C. Mudry, M. Sigrist, and W. Chen, Phys. Rev. B **96**, 205117 (2017).
[47] N. Schine, M. Chalupnik, T. Can, A. Gromov, and J. Simon, arXiv:1802.04418.
[48] N. P. Mitchell, L. M. Nash, D. Hexner, A. M. Turner, and W. T. Irvine, Nat. Phys. **14**, 380 (2018).
[49] W. S. Bakr, J. I. Gillen, A. Peng, S. Fölling, and M. Greiner, Nature **462**, 74 (2009).
[50] L. A. P. Ardila, M. Heyl, and A. Eckardt, arXiv:1806.08171.
[51] R. Bianco and R. Resta, Phys. Rev. Lett. **110**, 087202 (2013).
[52] F. Nathan, M. S. Rudner, N. H. Lindner, E. Berg, and G. Refael, Phys. Rev. Lett. **119**, 186801 (2017).

Acknowledgments. We are grateful for helpful conversations with Hannah Price, Lorenzo Privitera, Vincent Sacksteder and Michel Fruchart. This research was supported by the Netherlands Organisation for Scientific Research (NWO/OCW), an ERC Synergy Grant, EPSRC Grants EP/K030094/1 and EP/P009565/1, the Simons Foundation, and the Royal Society Grant No. UF120157. MDC and MJB thank the Thomas Young Centre and the Centre for Non-Equilibrium Science (CNES) at King's College London.

Author contributions. MDC performed the numerical simulations. All authors contributed to the analysis and writing of the manuscript.

Competing interests. The authors declare no competing interests.